

## MIT Open Access Articles

*Realization of 2D crystalline metal  
nitrides via selective atomic substitution*

The MIT Faculty has made this article openly available. **Please share**  
how this access benefits you. Your story matters.

**Citation:** Cao, Jun et al. "Realization of 2D crystalline metal nitrides via selective atomic substitution." Science Advances 6, 2 (January 2020): eaax8784.

**As Published:** 10.1126/SCIADV.AAX8784

**Publisher:** American Association for the Advancement of Science (AAAS)

**Persistent URL:** <https://hdl.handle.net/1721.1/129979>

**Version:** Final published version: final published article, as it appeared in a journal, conference proceedings, or other formally published context

**Terms of use:** Creative Commons Attribution NonCommercial License 4.0



## APPLIED SCIENCES AND ENGINEERING

## Realization of 2D crystalline metal nitrides via selective atomic substitution

Jun Cao<sup>1\*</sup>, Tianshu Li<sup>2\*</sup>, Hongze Gao<sup>2</sup>, Yuxuan Lin<sup>3</sup>, Xingzhi Wang<sup>1</sup>, Haozhe Wang<sup>3</sup>, Tomás Palacios<sup>3</sup>, Xi Ling<sup>1,2,4†</sup>

Two-dimensional (2D) transition metal nitrides (TMNs) are new members in the 2D materials family with a wide range of applications. Particularly, highly crystalline and large area thin films of TMNs are desirable for applications in electronic and optoelectronic devices; however, the synthesis of these TMNs has not yet been achieved. Here, we report the synthesis of few-nanometer thin Mo<sub>5</sub>N<sub>6</sub> crystals with large area and high quality via in situ chemical conversion of layered MoS<sub>2</sub> crystals. The versatility of this general approach is demonstrated by expanding the method to synthesize W<sub>5</sub>N<sub>6</sub> and TiN. Our strategy offers a new direction for preparing 2D TMNs with desirable characteristics, opening a door for studying fundamental physics and facilitating the development of next-generation electronics.

## INTRODUCTION

Transition metal nitrides (TMNs) are well-known for their high melting points, hardness, and chemical inertness (1, 2). The successful preparation of two-dimensional (2D) MXenes through selectively etching the “A” layer of bulk MAX phase triggered the study of 2D metal carbides and nitrides since 2011 (3–6). Although a variety of carbide MXenes have been synthesized using this method, the synthesis of nitrides MXenes is limited to Ti<sub>4</sub>N<sub>3</sub> and Ti<sub>2</sub>N (7, 8), due to the low availability of bulk MAXs for corresponding 2D metal nitrides. Urbankowski *et al.* (9) further reported the synthesis of multilayer molybdenum and vanadium nitrides by ammoniation of carbide MXenes synthesized using the selective etching method. Currently, as-synthesized 2D TMNs are either in solution phase or in powder form, and the lateral sizes of the flakes are usually small (<10 μm) (10–15). In addition, samples prepared by selective etching suffer from defects generated during the etching process and large thickness distributions (16, 17). These types of 2D TMNs are not suitable for high-performance electronic and optoelectronic device applications, which often require 2D crystals with decent area (>10 μm of lateral size), quality, and deposition on solid-state substrates (18, 19). Conventional 2D materials such as graphene and transition metal dichalcogenides (TMDs) produced using chemical vapor deposition (CVD) have made substantial progress in advancing the development of electronic devices (20–22). In contrast to many conventional 2D materials with strong in-plane covalent bonds and weak out-of-plane van der Waals interactions between the layers, the van der Waals gap is absent in bulk TMN crystals. Instead, covalent bonding extends in 3D frameworks of TMNs. Thus, conventional methods such as top-down mechanical exfoliation and bottom-up CVD, which take advantage of the weak interlayer van der Waals interaction and self-limited in-plane growth, are ineffective for the synthesis of

large-area and ultrathin 2D TMNs. Therefore, developing effective routes to synthesize 2D TMN crystals with desired morphology and quality is essential to realize the potential for applications toward electronic devices.

Using nitriding reaction of metal oxides, TMDs, and transition metal carbides (TMCs) to synthesize bulk TMNs is an established process (23–28). Recently, transformation of 2D MoS<sub>2</sub> and TMCs to 2D TMNs while retaining crystal structure was demonstrated in an ammonia atmosphere (9, 27). This transformation method is promising for large-area synthesis of 2D TMNs, considering the well-established preparation methods of TMD thin films with controlled thickness and various lateral dimensions ranging from micrometer size to wafer scale (22, 29, 30). However, the precursors used in the reported work for the transformation are either multilayered carbide MXenes or powder TMDs (9, 27). The obtained 2D TMNs are still marred by large thickness distributions, defective structures, and small lateral sizes passed on from the precursors. Moreover, an atomic-level investigation of the transformation, which is the key to evaluate the potential of the strategy for producing high-quality and large-area 2D TMN crystals, is lacking.

Here, beginning with a precursor layer of MoS<sub>2</sub>, an in situ transformation from MoS<sub>2</sub> to ultrathin Mo<sub>5</sub>N<sub>6</sub> is achieved. Optical and scanning electron microscopy (SEM) images show that the geometry and morphology of the crystals are retained during the transformation. The obtained Mo<sub>5</sub>N<sub>6</sub> exhibits high crystallinity over the entire area. In situ transformations of various MoS<sub>2</sub> flakes down to four layers for Mo<sub>5</sub>N<sub>6</sub> flakes with different thicknesses are achieved. Atomic force microscopy (AFM) analysis shows that the thickness of most of MoS<sub>2</sub> flakes is reduced by about two-third after the transformation. Electrical measurements show the high conductivity of metallic Mo<sub>5</sub>N<sub>6</sub> samples. We further demonstrate that this strategy can be applied to other TMDs such as WS<sub>2</sub> and TiS<sub>2</sub> for preparing their corresponding TMNs. This work opens a new direction for preparing 2D TMNs with desired quality that are previously inaccessible.

## RESULTS

Figure 1 shows a schematic illustration of the typical reaction process. The conversion was performed in a horizontal tube furnace

Copyright © 2020  
The Authors, some  
rights reserved;  
exclusive licensee  
American Association  
for the Advancement  
of Science. No claim to  
original U.S. Government  
Works. Distributed  
under a Creative  
Commons Attribution  
NonCommercial  
License 4.0 (CC BY-NC).

<sup>1</sup>Department of Chemistry, Boston University, 590 Commonwealth Avenue, Boston, MA 02215, USA. <sup>2</sup>Division of Materials Science and Engineering, Boston University, 15 St. Mary's Street, Boston, MA 02215, USA. <sup>3</sup>Department of Electrical Engineering and Computer Science, Massachusetts Institute of Technology, Cambridge, MA 02139, USA. <sup>4</sup>The Photonics Center, Boston University, 8 St. Mary's Street, Boston, MA 02215, USA.

\*These authors contributed equally to this work.

†Corresponding author. Email: xiling@bu.edu

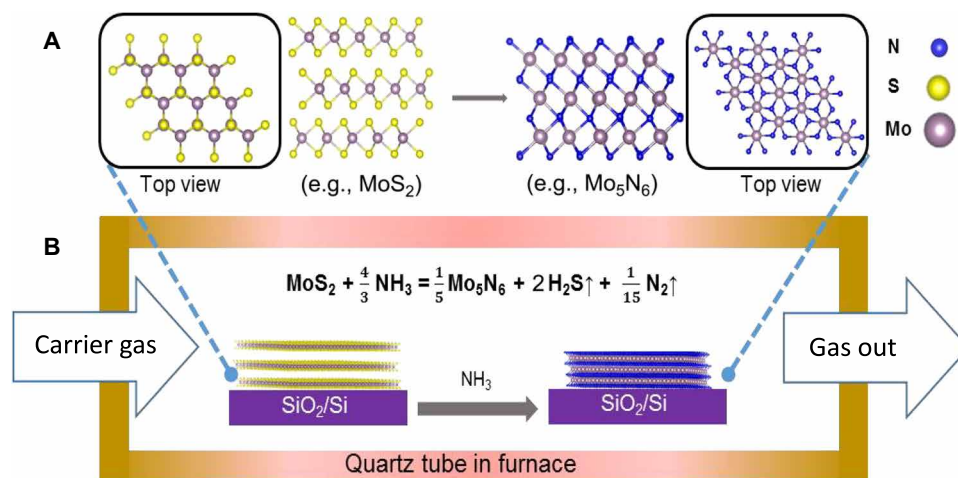
(see Materials and Methods for details of synthesis). MoS<sub>2</sub> flakes with different thicknesses were prepared using mechanical exfoliation and transferred onto a SiO<sub>2</sub>/Si substrate, which was then placed at the center of the furnace. A crucible filled with urea was placed in the upstream zone of the furnace, serving as the ammonia gas source, which was released from the thermolysis of urea at 200°C (31, 32). Ar gas (100 sccm) was used as carrier gas. The temperature in the center of the furnace was set at 750° to 800°C for the chemical reaction between gaseous ammonia and MoS<sub>2</sub> flakes (23, 27). Apart from Mo<sub>5</sub>N<sub>6</sub>, which was the solid product, the other two side products, H<sub>2</sub>S and N<sub>2</sub>, were in gaseous phase and carried away by the Ar gas (23, 27), leaving clean Mo<sub>5</sub>N<sub>6</sub> products with minimum contaminants.

Figure 2 (A and B) shows optical images of a 12.9-nm MoS<sub>2</sub> flake before and after the reaction. The optical contrast of the flake changed markedly after the reaction, but the morphology and shape of flakes are retained. Conversion results of more MoS<sub>2</sub> flakes with different thicknesses ranging from ~3 nm to tens of nanometers are shown in fig. S1. All MoS<sub>2</sub> flakes displayed notable changes of optical contrast after conversion. Absorption spectra (fig. S2) of the flake before (MoS<sub>2</sub>) and after (Mo<sub>5</sub>N<sub>6</sub>) the conversion suggest that such change originated from the distinct optical properties, consistent with the distinct electronic band structures of the two materials (15, 33). More evidence supporting the successful conversion of MoS<sub>2</sub> to Mo<sub>5</sub>N<sub>6</sub> is reported in later sections. AFM images show the atomically smooth surface of the flakes after conversion (fig. S3), suggesting a mild conversion process during which the reaction is confined within the original MoS<sub>2</sub> flakes. We further measured the Raman and photoluminescence (PL) spectra of the flake before and after the chemical transformation. As shown in Fig. 2C, pronounced A<sub>1g</sub> and E<sub>2g</sub> modes at ~384 and ~407 cm<sup>-1</sup> (34, 35) were observed from MoS<sub>2</sub> flakes before the transformation. Both modes vanished completely after the reaction, and new Raman peaks at ~215 and 710 cm<sup>-1</sup> appeared, indicating the transformation of the crystal domain. Similarly, PL from MoS<sub>2</sub> disappeared after the conversion (Fig. 2D) (33, 36), matching well with the semiconducting and metallic property of MoS<sub>2</sub> and Mo<sub>5</sub>N<sub>6</sub> (15, 33). In addition, Raman mapping results (Fig. 2, E and F) indicated that the entire flake was converted from MoS<sub>2</sub> to Mo<sub>5</sub>N<sub>6</sub>, where no Raman signals from MoS<sub>2</sub> were observed

on the converted flake globally. Corresponding PL mapping results are shown in fig. S4.

To determine the phase and crystal structure of the flake, we performed transmission electron microscopy (TEM) characterization on an as-prepared sample. The low-magnification TEM image in Fig. 3A shows the smooth surface of the flake where the small variations of the contrast are due to the wrinkles generated during the transfer process. The selected-area electron diffraction (SAED) pattern in Fig. 3B (see also fig. S5) indicates the high crystallinity of the sample. Same SAED pattern was observed when measuring on different regions of the flake. The hexagonal diffraction pattern is consistent with the crystal structure of the Mo<sub>5</sub>N<sub>6</sub> (15). The experimental and simulated SAED patterns (fig. S5) of Mo<sub>5</sub>N<sub>6</sub> match well with each other. High-angle annular dark-field (HAADF) scanning transmission electron microscopy (STEM) image is shown in Fig. 3C, where Mo atoms and atomic lattice are seen and no obvious defect is found in the sample. N atoms are invisible under our STEM condition due to the small atomic number compared to Mo atoms. In addition, the distance of 0.239 nm between the lattice planes is consistent with the d-spacing of (110) planes in Mo<sub>5</sub>N<sub>6</sub> crystal, which matches with the SAED pattern. We also noticed that the obtained Mo<sub>5</sub>N<sub>6</sub> crystal had an enhanced stability under 200-keV electron beam compared to MoS<sub>2</sub> flakes (37, 38), where Mo<sub>5</sub>N<sub>6</sub> flakes on TEM grid remained stable without noticeable change after being exposed under electron beam for 30 min (fig. S6), providing an additional advantage for future applications in electronic devices. STEM imaging and energy-dispersive spectroscopy (EDS) mapping were performed (see fig. S5) on a thick Mo<sub>5</sub>N<sub>6</sub> flake, which provides better signal-to-noise ratio of EDS signal. Dark-field STEM image shows the inhomogeneous contrast of the thick Mo<sub>5</sub>N<sub>6</sub> flake (fig. S5), which is probably due to strong local strain during the conversion process. EDS maps of N K peak and Mo L peak (fig. S5) show uniform distribution of Mo and N elements in the flake. The TEM characterization confirmed that a highly crystalline Mo<sub>5</sub>N<sub>6</sub> flake was successfully obtained through the chemical transformation.

The chemical composition and oxidation states of the elements in sample Mo<sub>5</sub>N<sub>6</sub> were characterized using x-ray photoelectron spectroscopy (XPS) and EDS analyses. Figure 3D shows the XPS wide scan survey spectrum of the sample, where notable Mo and



**Fig. 1. Schematic illustration of chemical conversion from MoS<sub>2</sub> to Mo<sub>5</sub>N<sub>6</sub>.** (A) Structural changes from MoS<sub>2</sub> to Mo<sub>5</sub>N<sub>6</sub>. (B) Schematics of the experimental setup for chemical conversion reactions.

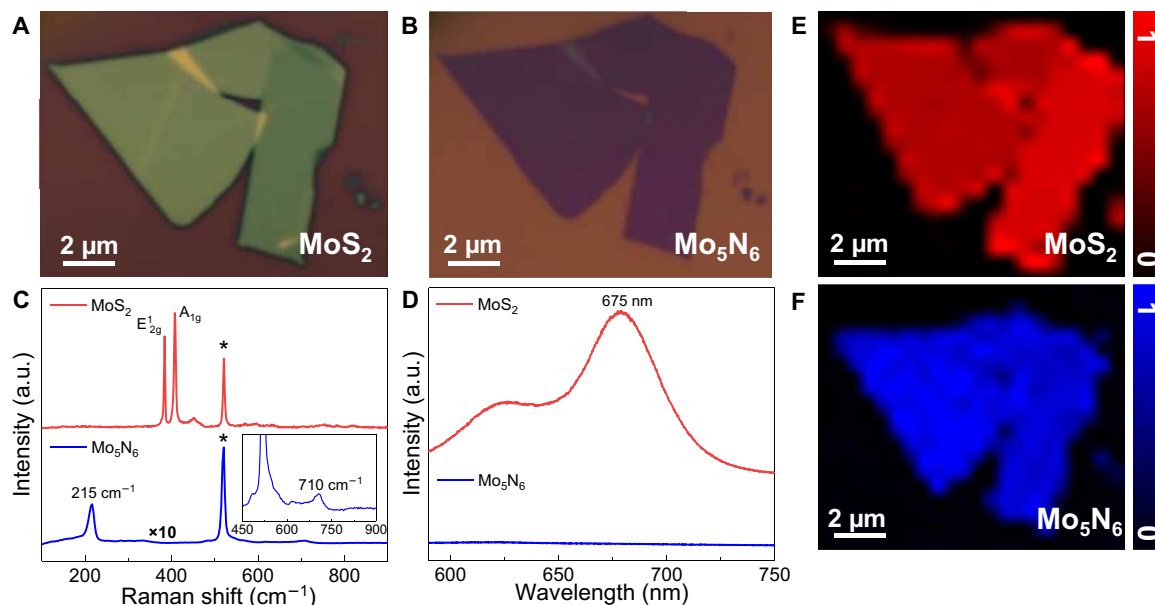


**Fig. 2. Typical optical microscope, Raman spectroscopy, and PL characterization of MoS<sub>2</sub> and Mo<sub>5</sub>N<sub>6</sub> flakes.** (A) Optical images of MoS<sub>2</sub> exfoliated on the SiO<sub>2</sub>/Si substrate. (B) Optical image of Mo<sub>5</sub>N<sub>6</sub> converted from MoS<sub>2</sub> in (A). (C) Comparison of Raman spectra of MoS<sub>2</sub> and Mo<sub>5</sub>N<sub>6</sub>. Peaks labeled with "\*" are from the SiO<sub>2</sub>/Si substrate. (D) Comparison of PL spectra of MoS<sub>2</sub> and Mo<sub>5</sub>N<sub>6</sub>. (E and F) Raman intensity maps of the A<sub>1g</sub> mode of MoS<sub>2</sub> (E) and the 215 cm<sup>-1</sup> mode of Mo<sub>5</sub>N<sub>6</sub> (F). Color bars show normalized Raman intensities, where "1" and "0" represent maximum and minimum intensity of Raman modes, respectively. a.u., arbitrary units.

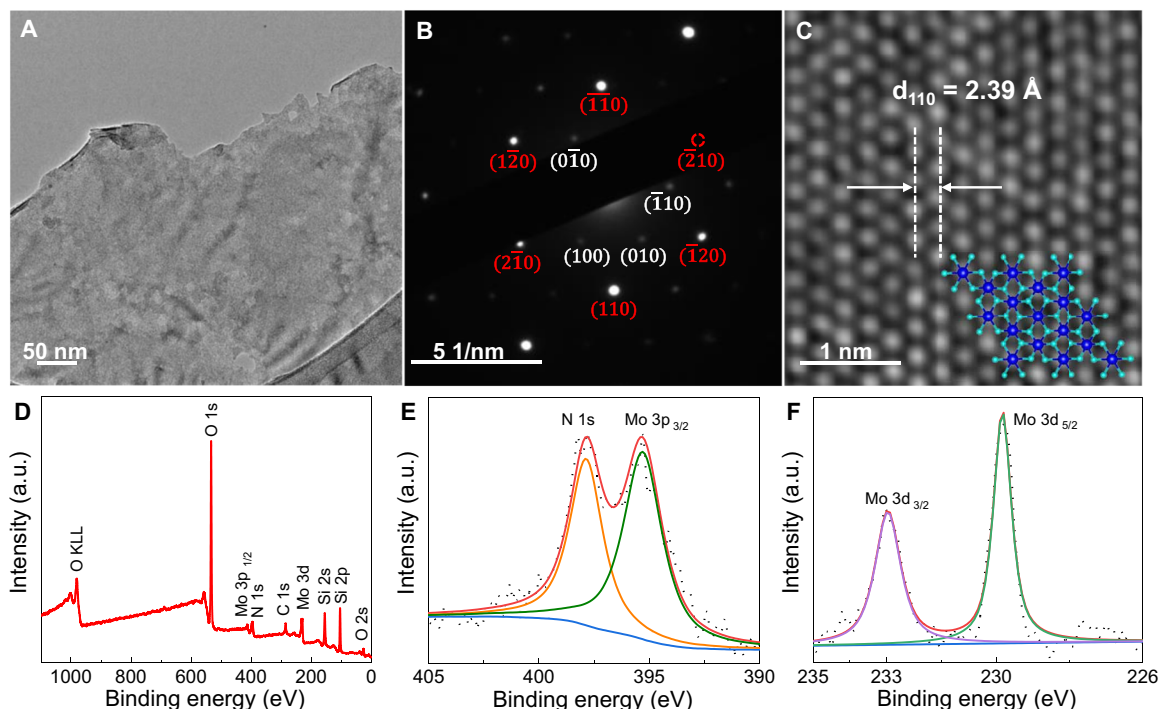


**Fig. 3. Crystal structure and elemental analysis of Mo<sub>5</sub>N<sub>6</sub> samples converted from MoS<sub>2</sub>.** (A) Low-magnification TEM image of Mo<sub>5</sub>N<sub>6</sub>. (B) SAED pattern taken by a 25 cm camera. Diffraction planes are labeled according to SAED simulation in fig. S4. Red circle corresponds to a diffraction plane blocked by TEM beam stop. (C) Filtered HAADF STEM image. Hexagonal Mo pattern is observed. Mo atoms and N atoms are labeled in blue and cyan color, respectively. (D) XPS survey spectrum of Mo<sub>5</sub>N<sub>6</sub>. (E and F) XPS spectra of Mo<sub>5</sub>N<sub>6</sub> in Mo 3p and N 1s region (E) and Mo 3d region (F).

N signals are observed and no signal from S appeared, indicating complete conversion of MoS<sub>2</sub> to Mo<sub>5</sub>N<sub>6</sub>. Other elements such as O, Si, and C are from the SiO<sub>2</sub>/Si substrate and the chamber environment. Similar results were obtained from EDS characterization (fig. S7).

High-resolution XPS spectra deconvolution for N 1s, Mo 3p, and Mo 3d regions are shown in Fig. 3 (E and F). The N 1s peak at 397.9 eV and Mo 3p<sub>3/2</sub> at 395.3 eV (Fig. 3E) suggest that chemical bond formed between Mo and N (15). In the Mo 3d region (Fig. 3F),



the peaks at 233.0 and 229.8 eV were assigned to the binding energies of Mo 3d<sub>3/2</sub> and Mo 3d<sub>5/2</sub>, respectively (39), with a spin-orbit splitting of 3.2 eV. This characteristic doublet of core-level Mo 3d<sub>5/2</sub> and 3d<sub>3/2</sub> indicates that Mo (+4) oxidation state dominates in Mo<sub>5</sub>N<sub>6</sub> (25). Nevertheless, the binding energy of 229.8 eV is slightly smaller than the reported value at 230.0 eV for Mo (+4) oxidation state (15), suggesting the coexistence of Mo (+3) oxidation state in the sample. No peaks corresponding to higher oxidation states of Mo from MoO<sub>x</sub> were observed in the Mo 3d region (40), ruling out the possibility of the formation of MoO<sub>x</sub>.

To address the mechanism by which the lattice changed during the atomic substitution from MoS<sub>2</sub> to Mo<sub>5</sub>N<sub>6</sub>, we investigated thickness changes of flakes before and after chemical conversion. The crystal structure models of MoS<sub>2</sub> and Mo<sub>5</sub>N<sub>6</sub> (Fig. 4, A and B) predict that the van der Waals gap between MoS<sub>2</sub> layers will disappear during the transformation to Mo<sub>5</sub>N<sub>6</sub> crystals, leading to the reducing of the thickness from MoS<sub>2</sub> to Mo<sub>5</sub>N<sub>6</sub>. The distance between two Mo layers in MoS<sub>2</sub> is 7.66 Å (41), while it is 2.77 Å in Mo<sub>5</sub>N<sub>6</sub> (42); therefore, the thickness of the flake can be predicted to decrease to 36% when transforming from MoS<sub>2</sub> to Mo<sub>5</sub>N<sub>6</sub>. To test this hypothesis, we performed AFM to extract the thickness of flakes. As expected, we observed that the thickness was reduced after chemical transformation. Figure 4 (C and D) shows typical AFM images of MoS<sub>2</sub> and corresponding Mo<sub>5</sub>N<sub>6</sub> flake, where they have nearly the same morphology and both surfaces are smooth. However, the thickness of the flake decreased from 9.5 nm for MoS<sub>2</sub> to 3.5 nm for Mo<sub>5</sub>N<sub>6</sub> (Fig. 4E), where Mo<sub>5</sub>N<sub>6</sub>/MoS<sub>2</sub> thickness ratio is 37%. Furthermore, we performed this comparison for ~30 flakes with MoS<sub>2</sub> thickness ranging from a few nanometers to ~35 nm. Reduced sample thickness was observed for all flakes after conversion (Fig. 4F). The average Mo<sub>5</sub>N<sub>6</sub>/MoS<sub>2</sub> thickness ratio is 56% based on the slope of linear fitting curve, but for

MoS<sub>2</sub> flakes with the thickness of 5 to 15 nm, the ratio is around 40%, matching well with the expected value. For thinner flakes, the ratio is larger, probably because the termination groups on the surface are non-negligible at this size range (3, 5) or the substrate roughness introduces a large uncertainty for the measurement. Figure S8 shows that a four-layer MoS<sub>2</sub> flake (3.4 nm) turned to a 2.1 nm Mo<sub>5</sub>N<sub>6</sub> flake after conversion. Note that we found that the morphology and quality of the flake remain well at such thin level. On the basis of the morphology retaining and thickness depression phenomena observed in our experiments, we propose the following mechanism of the chemical transformation from MoS<sub>2</sub> to Mo<sub>5</sub>N<sub>6</sub>. When NH<sub>3</sub> gas diffuses into the van der Waals gaps of the MoS<sub>2</sub> flake, one N atom will replace two S atoms sandwiched by two adjacent Mo layers. When Mo—S bonds around a Mo atom are broken, six binding sites on the Mo atom will be released. Each N atom will then bond with six Mo atoms to form Mo<sub>5</sub>N<sub>6</sub>, where adjacent Mo layers are bridged by the N atoms, leading to the vanishing of the van der Waals gaps that originally exist in MoS<sub>2</sub>. In this process, breaking Mo—S bonds and forming Mo—N bonds do not require large rearrangements of Mo atoms, although small shift of positions of Mo atoms may be necessary to compensate the bond length difference between Mo—S and Mo—N. Despite the layered structure of MoS<sub>2</sub> (point group, D<sub>6h</sub>; space group, P6<sub>3</sub>/mmc) (41) and nonlayered nature of Mo<sub>5</sub>N<sub>6</sub> (point group, C<sub>6h</sub>; space group, P6<sub>3</sub>/m) (42), the Mo layers in these two materials are both in hexagonal pattern. This similarity in structure allows gentle transformation without structural collapse, leading to the morphology retaining of samples before and after chemical transformation.

To further investigate the transformation process, we performed the reaction under varying conditions. We found that excess amount of urea, which provided sufficient NH<sub>3</sub> gas in the chamber, was a

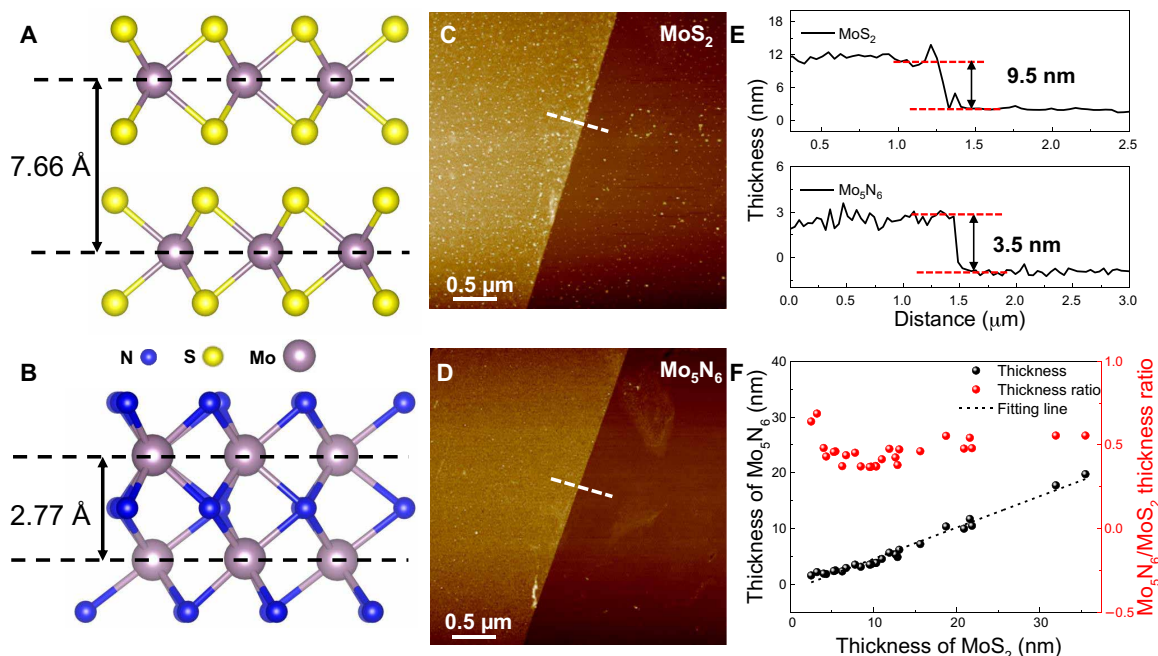


**Fig. 4. Thickness characterization and analysis of samples before (MoS<sub>2</sub>) and after conversion (Mo<sub>5</sub>N<sub>6</sub>).** (A and B) Side view of crystal structures labeled with distance between adjacent Mo layers in MoS<sub>2</sub> and Mo<sub>5</sub>N<sub>6</sub>. (C and D) AFM images of the same flake before [MoS<sub>2</sub> (C)] and after conversion [Mo<sub>5</sub>N<sub>6</sub> (D)]. The white dashed lines indicate the location where we measured the thickness of the flakes. (E) AFM height profiles of the flake before [MoS<sub>2</sub> (C)] and after conversion [Mo<sub>5</sub>N<sub>6</sub> (D)]. (F) Correlation plot of the thickness of MoS<sub>2</sub> and converted Mo<sub>5</sub>N<sub>6</sub> (in black). Data points in red show the corresponding thickness ratios of Mo<sub>5</sub>N<sub>6</sub>/MoS<sub>2</sub>.

key factor for the success because it ensured a reducing environment to prevent MoS<sub>2</sub> from oxidation (fig. S9). In addition, the degree of conversion could be tuned by changing the reaction temperature and time. A complete conversion occurred within 5 min when the reaction temperature varied from 750° to 800°C (fig. S9). However, at 700°C, the conversion was only partially complete even after 60 min, where only the edge area was converted and no Mo<sub>5</sub>N<sub>6</sub> was observed in the central region of the flake (fig. S10), indicating that the conversion started from the edge of the MoS<sub>2</sub> flake. Because of the partial conversion, we realized a lateral heterostructure between MoS<sub>2</sub> and Mo<sub>5</sub>N<sub>6</sub> through a simple partial conversion. The successful synthesis of this heterostructure offers a great platform for future study on the junction properties and applications. Moreover, the converted Mo<sub>5</sub>N<sub>6</sub> showed excellent stability, where the crystal structure remained intact after 6 months and survived in acetone, deionized (DI) water, and 1 M H<sub>2</sub>SO<sub>4</sub> solution for at least 2 hours without noticeable changes from optical images and Raman spectra (fig. S11). This is advantageous to be compatible with future device fabrication process.

To examine the electrical property of the converted Mo<sub>5</sub>N<sub>6</sub> sample, we fabricated a back-gate transport device on a 9.5 nm-thick Mo<sub>5</sub>N<sub>6</sub> flake (Fig. 5A and fig. S13). The gate dependence of the transport current shows that the drain-source current ( $I_{ds}$ ) remained constant as the gate voltage scanned from -20 to 20 V, and variations of  $I_{ds}$  was still negligible even when noise signal became visible, featuring metallic behavior of the as-synthesized Mo<sub>5</sub>N<sub>6</sub> sample (Fig. 5B). We further performed the temperature-dependent transport measurement down to 77 K to investigate the electrical conductivity of the sample. Fig. 5C shows the output current-voltage relation ( $I$ - $V$ ) characteristics through a four-probe measurement, where the slope of the

$I$ - $V$  curves increases very slowly as the temperature increases from 77 to 240 K (Fig. 5C, inset). The sheet resistances of Mo<sub>5</sub>N<sub>6</sub> at different temperatures were extracted from the slope of  $I$ - $V$  curves and the dimension of the transport device (Fig. 5D), using the formula  $R_s = R \times (W/L)$ .  $R$  is the total electrical resistance of the device, and  $W$  and  $L$  are the effective width and length of the measurement area, which are measured as 3.4 and 6.1  $\mu\text{m}$ , respectively, from the optical image. Low sheet resistances of Mo<sub>5</sub>N<sub>6</sub> ranging from 114.4 to 117.8 ohm square<sup>-1</sup> were obtained under different temperatures, which is in the same order of magnitude of CVD graphene (43). The fact that the sheet resistance of Mo<sub>5</sub>N<sub>6</sub> is not sensitive to the temperature change from 77 and 240 K is consistent with the trend of TMNs reported in the literature (9).

We further applied this strategy to the conversion from WS<sub>2</sub> and TiS<sub>2</sub> to their corresponding nitrides (see Materials and Methods for details of the synthetic conditions). Figure 6 shows a typical conversion result on a 5.6 nm WS<sub>2</sub> and a ~100 nm TiS<sub>2</sub> flake. As shown in Fig. 6 (A to H), distinct optical contrast change was observed from WS<sub>2</sub> and WS<sub>2</sub>N<sub>6</sub>, as well as from TiS<sub>2</sub> to TiN. Similar to the case of MoS<sub>2</sub> to Mo<sub>5</sub>N<sub>6</sub> conversion, the morphology of the flakes was retained. Raman characterization showed that the Raman signatures from WS<sub>2</sub> and TiS<sub>2</sub> disappeared completely (44, 45). Instead, new peaks that correspond to the phonon modes of WS<sub>2</sub>N<sub>6</sub> (e.g., ~258 cm<sup>-1</sup>) and TiN (e.g., ~154 and 620 cm<sup>-1</sup>) (46, 47) appeared (Fig. 6, I to J), indicating a successful chemical conversion. The Raman mapping results show that the conversion is thorough and uniform. More optical and corresponding SEM images of WS<sub>2</sub>N<sub>6</sub> (fig. S12) and TiN (fig. S12) corroborate uniform surface of converted samples. Phase and crystallinity of WS<sub>2</sub>N<sub>6</sub> are characterized by HRTEM and EDS analyses (fig. S14) (48). Similar to Mo<sub>5</sub>N<sub>6</sub>, WS<sub>2</sub>N<sub>6</sub> and TiN also exhibit

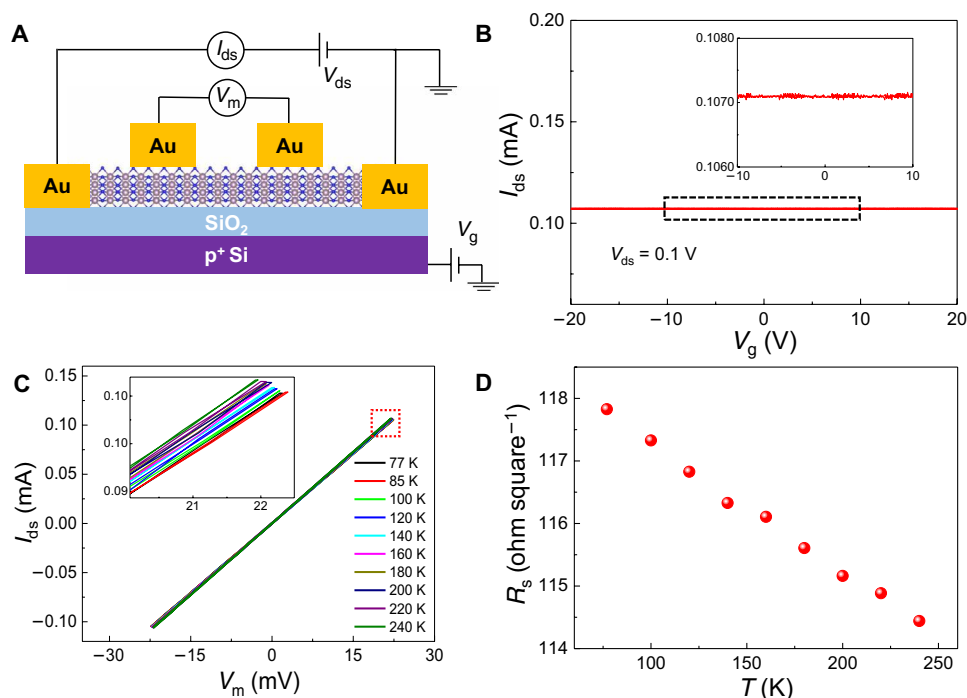


**Fig. 5. Electrical transport measurements of Mo<sub>5</sub>N<sub>6</sub>.** (A) Schematics of a back-gate device together with electrical connections. (B) Transfer curve of Mo<sub>5</sub>N<sub>6</sub> transport device for both forward and reverse  $V_g$  bias with back-gate modulations. Inset: Zoomed-in image of the area indicated by the black rectangle. Negligible gate dependence of the  $I_{ds}$  is observed in Mo<sub>5</sub>N<sub>6</sub> transport device. (C) Output  $I$ - $V$  curve of Mo<sub>5</sub>N<sub>6</sub> transport device under different temperatures at zero gate voltage. Inset: Zoomed-in region of the  $I$ - $V$  curve indicated by the red square. (D) Temperature dependence of the sheet resistance of the Mo<sub>5</sub>N<sub>6</sub> sample.

excellent stability against acetone, DI water, and 1 M  $\text{H}_2\text{SO}_4$  for at least 2 hours (fig. S11).

## DISCUSSION

We demonstrate a versatile conversion strategy from layered TMDs to their corresponding ultrathin nitrides through atomic substitution from chalcogen to nitrogen. This method facilitates the production of 2D crystalline TMNs including  $\text{Mo}_5\text{N}_6$ ,  $\text{W}_5\text{N}_6$ , and  $\text{TiN}$ , offering a pathway toward an important class of 2D materials that previously are inaccessible. The investigation of the in situ transformation from  $\text{MoS}_2$  layers to 2D  $\text{Mo}_5\text{N}_6$  crystals shows reduced thickness after conversion. 2D  $\text{Mo}_5\text{N}_6$  crystal as thin as 2.1 nm is achieved by converting a four-layer  $\text{MoS}_2$ . The electrical measurement shows that the converted  $\text{Mo}_5\text{N}_6$  is metallic with high conductivity, where the sheet resistance is as low as  $100 \text{ ohm square}^{-1}$ . By controlling the reaction rate, we achieve a  $\text{Mo}_5\text{N}_6$ - $\text{MoS}_2$  lateral heterostructure, demonstrating the advantage of our method in integrating 2D materials together for basic building blocks (e.g., metal-semiconductor junction) for future applications in electronic devices. Building on

the success of the TMDs synthesis in the field (21, 22, 30), we anticipate that the strategy we report here will lead to effective synthesis of large-area and high-quality 2D TMNs that satisfy the needs for high-performance electronic and optoelectronic devices.

## MATERIALS AND METHODS

### Conversion from TMDs to TMNs

$\text{MoS}_2$ ,  $\text{WS}_2$ , and  $\text{TiS}_2$  with different thicknesses were prepared using mechanical exfoliation method from their bulk crystals (purchased from HQ Graphene) and transferred onto 300 nm  $\text{SiO}_2/\text{Si}$  substrates. Note that  $\text{SiO}_2/\text{Si}$  substrates were cleaned by sonication in water, acetone, and isopropanol solvents sequentially (each for 10 min), followed by  $\text{O}_2$  plasma cleaning before use. Chemical conversions were conducted in a horizontal tube furnace where Ar gas was introduced into the tube and the flow was controlled by a mass flow controller. Samples were placed in a 2.5-cm-diameter quartz tube in the center of the furnace. Excess amount of urea (500 mg) was placed in an  $\text{Al}_2\text{O}_3$  crucible located upstream of the furnace, serving as nitrogen source. After purging with Ar gas for 10 mins, the tube was heated

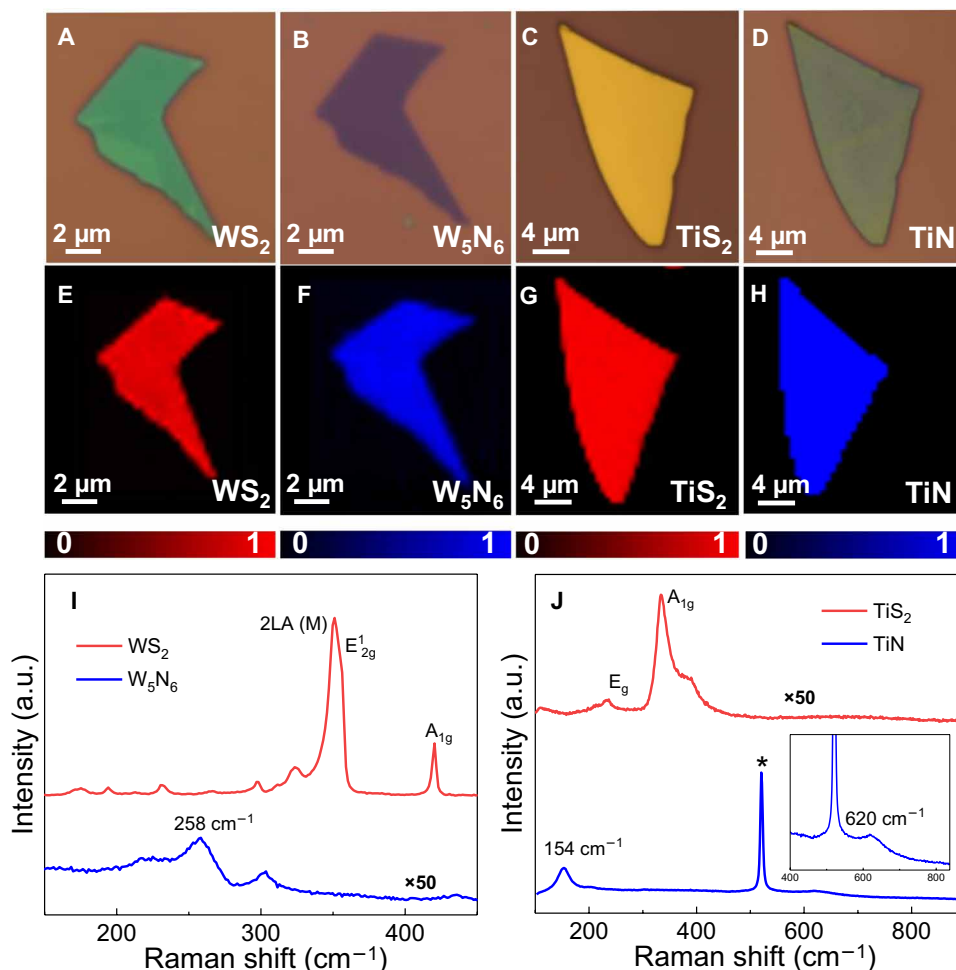


**Fig. 6. Conversion on  $\text{WS}_2$  and  $\text{TiS}_2$  for  $\text{W}_5\text{N}_6$  and  $\text{TiN}$ .** (A to D) Optical images of  $\text{WS}_2$  (A),  $\text{W}_5\text{N}_6$  (B),  $\text{TiS}_2$  (C), and  $\text{TiN}$  (D). (E to H) Raman intensity maps of  $\text{E}_{12g}$  mode of  $\text{WS}_2$  (E),  $258 \text{ cm}^{-1}$  mode of  $\text{W}_5\text{N}_6$  (F),  $\text{A}_{1g}$  mode of  $\text{TiS}_2$  (G), and  $154 \text{ cm}^{-1}$  mode of  $\text{TiN}$  (H). Color bars show normalized Raman intensities, where “1” and “0” represent maximum and minimum intensity of Raman modes, respectively. (I and J) Comparison of Raman spectra of  $\text{WS}_2$  and  $\text{W}_5\text{N}_6$  (I) and  $\text{TiS}_2$  and  $\text{TiN}$  (J). Peak labeled with “\*” is from the  $\text{SiO}_2/\text{Si}$  substrate.

to 800°C with a 30 min ramp. The conversion time for Mo<sub>5</sub>N<sub>6</sub> and TiN is 1 and 2 hours for W<sub>5</sub>N<sub>6</sub>. Throughout the conversion, 100 sccm Ar flow was used to maintain the inert atmosphere. When conversion was completed, the system was cooled down naturally.

### Material characterizations

As-prepared TMNs were characterized using Raman spectroscopy, AFM, TEM, STEM, SAED XPS, and EDS. Raman and PL measurements were performed on a Renishaw inVia Raman microscope equipped with a 532 nm laser line. All the spectra in comparison were taken using the same condition. The AFM topography was acquired on a Bruker Dimension system. TEM measurements were performed on a FEI Tecnai Osiris TEM, operating at a 200 keV accelerating voltage. SAED was measured on a JEOL 2100 TEM. The SAED simulation was performed through STEM\_CELL software (49). Atomic-resolution STEM and EDS mapping was performed on a JEOL ARM 200F STEM, operating at 200 keV. XPS measurements were performed using a PHI Versaprobe II.

### Fabrication and conductivity measurements

The electrical transport device was fabricated through laser writer lithography and thermal evaporation of 5 nm Cr and 45 nm Au. For lift-off, the sample was soaked in Remover PG at 60°C for 10 min to remove the photoresist and then washed in isopropanol and DI water. Device characterization was performed using a semiconductor parameter analyzer (Keysight B1500A) and a Lakeshore cryogenic probe station with micromanipulation probes and liquid nitrogen cooling. All measurements were performed in vacuum ( $<3 \times 10^{-6}$  torr).

### SUPPLEMENTARY MATERIALS

Supplementary material for this article is available at <http://advances.sciencemag.org/cgi/content/full/6/2/eaax8784/DC1>

- Fig. S1. Typical optical images of MoS<sub>2</sub> and Mo<sub>5</sub>N<sub>6</sub> flakes with different thicknesses.
- Fig. S2. Absorption spectra of MoS<sub>2</sub> and Mo<sub>5</sub>N<sub>6</sub> samples on quartz substrate.
- Fig. S3. AFM images of MoS<sub>2</sub> and Mo<sub>5</sub>N<sub>6</sub> flakes in Fig. 2.
- Fig. S4. PL intensity maps of MoS<sub>2</sub> and Mo<sub>5</sub>N<sub>6</sub> flake.
- Fig. S5. Structural and elemental characterizations of Mo<sub>5</sub>N<sub>6</sub>.
- Fig. S6. TEM images of Mo<sub>5</sub>N<sub>6</sub> sample under 200-keV electron beam.
- Fig. S7. EDS spectrum of Mo<sub>5</sub>N<sub>6</sub>.
- Fig. S8. Optical, AFM, and SEM images of chemical transformation on a four-layer MoS<sub>2</sub> flake.
- Fig. S9. Optical images of Mo<sub>5</sub>N<sub>6</sub> flakes prepared from chemical transformations under different conditions.
- Fig. S10. Optical images and Raman spectra of a partially converted flake at 700°C.
- Fig. S11. Stability test of Mo<sub>5</sub>N<sub>6</sub>, W<sub>5</sub>N<sub>6</sub>, and TiN.
- Fig. S12. Optical and SEM images of WS<sub>2</sub>, W<sub>5</sub>N<sub>6</sub>, TiS<sub>2</sub>, and TiN flakes.
- Fig. S13. Optical and AFM images of Mo<sub>5</sub>N<sub>6</sub> transport device.
- Fig. S14. TEM and EDS characterizations of W<sub>5</sub>N<sub>6</sub> converted from WS<sub>2</sub>.

### REFERENCES AND NOTES

1. L. E. Toth, *Transition Metal Carbides and Nitrides* (Academic Press, 1971).
2. H. A. Pierson, *Handbook of Refractory Carbides and Nitrides* (Noyes, 1996).
3. M. Naguib, M. Kurtoglu, V. Presser, J. Lu, J. Niu, M. Heon, L. Hultman, Y. Gogotsi, M. W. Barsoum, Two-dimensional nanocrystals produced by exfoliation of Ti<sub>3</sub>AlC<sub>2</sub>. *Adv. Mater.* **23**, 4248–4253 (2011).
4. M. R. Lukatskaya, O. Mashtalir, C. E. Ren, Y. Dall'Agnese, P. Rozier, P. L. Taberna, M. Naguib, P. Simon, M. W. Barsoum, Y. Gogotsi, Cation intercalation and high volumetric capacitance of two-dimensional titanium carbide. *Science* **341**, 1502–1505 (2013).
5. B. Anasori, M. R. Lukatskaya, Y. Gogotsi, 2D metal carbides and nitrides (MXenes) for energy storage. *Nat. Rev. Mater.* **2**, 16098 (2017).
6. K. Hantanasirisakul, Y. Gogotsi, Electronic and optical properties of 2D transition metal carbides and nitrides (MXenes). *Adv. Mater.* **30**, 1804779 (2018).
7. P. Urbankowski, B. Anasori, T. Makaryan, D. Er, S. Kota, P. L. Walsh, M. Zhao, V. B. Shenoy, M. W. Barsoum, Y. Gogotsi, Synthesis of two-dimensional titanium nitride Ti<sub>4</sub>N<sub>3</sub> (MXene). *Nanoscale* **8**, 11385–11391 (2016).
8. B. Soundiraraju, B. K. George, Two-dimensional titanium nitride (Ti<sub>2</sub>N) MXene: Synthesis, characterization, and potential application as surface-enhanced Raman scattering substrate. *ACS Nano* **11**, 8892–8900 (2017).
9. P. Urbankowski, B. Anasori, K. Hantanasirisakul, L. Yang, L. Zhang, B. Haines, S. J. May, S. J. L. Billinge, Y. Gogotsi, 2D molybdenum and vanadium nitrides synthesized by ammoniation of 2D transition metal carbides (MXenes). *Nanoscale* **9**, 17722–17730 (2017).
10. M. Naguib, O. Mashtalir, J. Carle, V. Presser, J. Lu, L. Hultman, Y. Gogotsi, M. W. Barsoum, Two-dimensional transition metal carbides. *ACS Nano* **6**, 1322–1331 (2012).
11. B. Anasori, Y. Xie, M. Beidaghi, J. Lu, B. C. Hosler, L. Hultman, P. R. C. Kent, Y. Gogotsi, M. W. Barsoum, Two-dimensional, ordered, double transition metals carbides (MXenes). *ACS Nano* **9**, 9507–9516 (2015).
12. A. Lipatov, M. Alhabeb, M. R. Lukatskaya, A. Bosen, Y. Gogotsi, A. Sinitiskii, Effect of synthesis on quality, electronic properties and environmental stability of individual monolayer Ti<sub>3</sub>C<sub>2</sub> MXene flakes. *Adv. Electron. Mater.* **2**, 1600255 (2016).
13. F. Shahzad, M. Alhabeb, C. B. Hatter, B. Anasori, S. Man Hong, C. M. Koo, Y. Gogotsi, Electromagnetic interference shielding with 2D transition metal carbides (MXenes). *Science* **353**, 1137–1140 (2016).
14. Y.-Y. Peng, B. Akuzum, N. Kurra, M.-Q. Zhao, M. Alhabeb, B. Anasori, E. C. Kumbur, H. N. Alshareef, M.-D. Ger, Y. Gogotsi, All-MXene (2D titanium carbide) solid-state microsupercapacitors for on-chip energy storage. *Energ. Environ. Sci.* **9**, 2847–2854 (2016).
15. H. Jin, X. Liu, A. Vasileff, Y. Jiao, Y. Zhao, Y. Zheng, S.-Z. Qiao, Single-crystal nitrogen-rich two-dimensional Mo<sub>5</sub>N<sub>6</sub> nanosheets for efficient and stable seawater splitting. *ACS Nano* **12**, 12761–12769 (2018).
16. L. H. Karlsson, J. Birch, J. Halim, M. W. Barsoum, P. O. Å. Persson, Atomically resolved structural and chemical investigation of single MXene sheets. *Nano Lett.* **15**, 4955–4960 (2015).
17. X. Sang, Y. Xie, M.-W. Lin, M. Alhabeb, K. L. Van Aken, Y. Gogotsi, P. R. C. Kent, K. Xiao, R. R. Unocic, Atomic defects in monolayer titanium carbide (Ti<sub>3</sub>C<sub>2</sub>T<sub>x</sub>) MXene. *ACS Nano* **10**, 9193–9200 (2016).
18. L. Yu, Y.-H. Lee, X. Ling, E. J. G. Santos, Y. C. Shin, Y. Lin, M. Dubey, E. Kaxiras, J. Kong, H. Wang, T. Palacios, Graphene/MoS<sub>2</sub> hybrid technology for large-scale two-dimensional electronics. *Nano Lett.* **14**, 3055–3063 (2014).
19. Y.-C. Lin, B. Jariwala, B. Bersch, K. Xu, Y. Nie, B. Wang, S. M. Eichfeld, X. Zhang, T. H. Choudhury, Y. Pan, R. Addou, C. M. Smyth, J. Li, K. Zhang, M. A. Haque, S. Fölsch, R. M. Feenstra, R. M. Wallace, K. Cho, S. K. Fullerton-Shirey, J. M. Redwing, J. A. Robinson, Realizing large-scale, electronic-grade two-dimensional semiconductors. *ACS Nano* **12**, 965–975 (2018).
20. X. Li, W. Cai, J. An, S. Kim, J. Nah, D. Yang, R. Piner, A. Velamakanni, I. Jung, E. Tutuc, S. K. Banerjee, L. Colombo, R. S. Ruoff, Large-area synthesis of high-quality and uniform graphene films on copper foils. *Science* **324**, 1312–1314 (2009).
21. X. Ling, Y.-H. Lee, Y. Lin, W. Fang, L. Yu, M. S. Dresselhaus, J. Kong, Role of the seeding promoter in MoS<sub>2</sub> growth by chemical vapor deposition. *Nano Lett.* **14**, 464–472 (2014).
22. Z. Cai, B. Liu, X. Zou, H.-M. Cheng, Chemical vapor deposition growth and applications of two-dimensional materials and their heterostructures. *Chem. Rev.* **118**, 6091–6133 (2018).
23. S. T. Oyama, *The Chemistry of Transition Metal Carbides and Nitrides*, S. T. Oyama, Ed. (Blackie Academic and Professional, 1996).
24. C. Giordano, C. Erpen, W. Yao, M. Antonietti, Synthesis of Mo and W carbide and nitride nanoparticles via a simple “urea glass” route. *Nano Lett.* **8**, 4659–4663 (2008).
25. J. Liu, S. Tang, Y. Lu, G. Cai, S. Liang, W. Wang, X. Chen, Synthesis of Mo<sub>2</sub>N nanolayer coated MoO<sub>3</sub> hollow nanostructures as high-performance anode materials for lithium-ion batteries. *Energ. Environ. Sci.* **6**, 2691–2697 (2013).
26. M. B. Sreedhara, K. Vasu, C. N. R. Rao, Synthesis and characterization of few-layer nanosheets of GaN and other metal nitrides. *Z. anorg. allg. Chemie.* **640**, 2737–2741 (2014).
27. G.-D. Sun, G.-H. Zhang, K.-C. Chou, Synthesis of molybdenum nitrides nanosheets by nitriding 2H-MoS<sub>2</sub> with ammonia. *J. Am. Ceram. Soc.* **101**, 2796–2808 (2018).
28. X. Xiao, H. Wang, P. Urbankowski, Y. Gogotsi, Topochemical synthesis of 2D materials. *Chem. Soc. Rev.* **47**, 8744–8765 (2018).
29. K. S. Novoselov, D. Jiang, F. Schedin, T. J. Booth, V. V. Khotkevich, S. V. Morozov, A. K. Geim, Two-dimensional atomic crystals. *Proc. Natl. Acad. Sci. U.S.A.* **102**, 10451–10453 (2005).
30. K. Kang, S. Xie, L. Huang, Y. Han, P. Y. Huang, K. F. Mak, C.-J. Kim, D. Muller, J. Park, High-mobility three-atom-thick semiconducting films with wafer-scale homogeneity. *Nature* **520**, 656–660 (2015).
31. S. D. Yim, S. J. Kim, J. H. Baik, I.-S. Nam, Y. S. Mok, J.-H. Lee, B. K. Cho, S. H. Oh, Decomposition of urea into NH<sub>3</sub> for the SCR process. *Ind. Eng. Chem. Res.* **43**, 4856–4863 (2004).
32. A. Lundström, B. Andersson, L. Olsson, Urea thermolysis studied under flow reactor conditions using DSC and FT-IR. *Chem. Eng. J.* **150**, 544–550 (2009).
33. A. Splendiani, L. Sun, Y. Zhang, T. Li, J. Kim, C.-Y. Chim, G. Galli, F. Wang, Emerging photoluminescence in monolayer MoS<sub>2</sub>. *Nano Lett.* **10**, 1271–1275 (2010).



34. T. J. Wieting, J. L. Verble, Infrared and raman studies of long-wavelength optical phonons in hexagonal MoS<sub>2</sub>. *Phys. Rev. B* **3**, 4286–4292 (1971).
35. J. L. Verble, T. J. Wieting, Lattice mode degeneracy in MoS<sub>2</sub> and other layer compounds. *Phys. Rev. Lett.* **25**, 362–365 (1970).
36. G. Eda, H. Yamaguchi, D. Voiry, T. Fujita, M. Chen, M. Chhowalla, Photoluminescence from chemically exfoliated MoS<sub>2</sub>. *Nano Lett.* **11**, 5111–5116 (2011).
37. A. Garcia, A. M. Raya, M. M. Mariscal, R. Esparza, M. Herrera, S. I. Molina, G. Scavello, P. L. Galindo, M. Jose-Yacamán, A. Ponce, Analysis of electron beam damage of exfoliated MoS<sub>2</sub> sheets and quantitative HAADF-STEM imaging. *Ultramicroscopy* **146**, 33–38 (2014).
38. R. Zan, Q. M. Ramasse, R. Jalil, T. Georgiou, U. Bangert, K. S. Novoselov, Control of radiation damage in MoS<sub>2</sub> by graphene encapsulation. *ACS Nano* **7**, 10167–10174 (2013).
39. L. Zhang, X. Ji, X. Ren, Y. Ma, X. Shi, Z. Tian, A. M. Asiri, L. Chen, B. Tang, X. Sun, Electrochemical ammonia synthesis via nitrogen reduction reaction on a MoS<sub>2</sub> catalyst: Theoretical and experimental studies. *Adv. Mater.* **30**, 1800191 (2018).
40. C. Martella, P. Melloni, E. Cinquanta, E. Ciani, M. Alia, M. Longo, A. Lamperti, S. Vangelista, M. Fanciulli, A. Molle, Engineering the growth of MoS<sub>2</sub> via atomic layer deposition of molybdenum oxide film precursor. *Adv. Electron. Mater.* **2**, 1600330 (2016).
41. E. S. Kadantsev, P. Hawrylak, Electronic structure of a single MoS<sub>2</sub> monolayer. *Solid State Commun.* **152**, 909–913 (2012).
42. A. Y. Ganin, L. Kienle, G. V. Vajenine, Synthesis and characterisation of hexagonal molybdenum nitrides. *J. Solid State Chem.* **179**, 2339–2348 (2006).
43. F. Bonaccorso, Z. Sun, T. Hasan, A. C. Ferrari, Graphene photonics and optoelectronics. *Nat. Photonics* **4**, 611–622 (2010).
44. M. Thirupuranthaka, R. V. Kashid, C. Sekhar Rout, D. J. Late, Temperature dependent Raman spectroscopy of chemically derived few layer MoS<sub>2</sub> and WS<sub>2</sub> nanosheets. *Appl. Phys. Lett.* **104**, 081911 (2014).
45. C. J. Carmalt, S. A. O'Neill, I. P. Parkin, E. S. Peters, Titanium sulfide thin films from the aerosol-assisted chemical vapour deposition of [Ti(SBu)<sub>3</sub>]<sub>4</sub>. *J. Mater. Chem.* **14**, 830–834 (2004).
46. C. C. Chen, N. T. Liang, W. S. Tse, I. Y. Chen, J. G. Duh, Raman spectra of titanium nitride thin films. *Chinese J. Phys.* **32**, 205 (1994).
47. S. Yu, Q. Zeng, A. R. Oganov, G. Frapper, L. Zhang, Phase stability, chemical bonding and mechanical properties of titanium nitrides: A first-principles study. *Phys. Chem. Chem. Phys.* **17**, 11763–11769 (2015).
48. Z. Zhao, K. Bao, D. Duan, F. Tian, Y. Huang, H. Yu, Y. Liu, B. Liu, T. Cui, The low coordination number of nitrogen in hard tungsten nitrides: A first-principles study. *Phys. Chem. Chem. Phys.* **17**, 13397–13402 (2015).
49. V. Grillo, E. Rotunno, STEM\_CELL: A software tool for electron microscopy: Part I—Simulations. *Ultramicroscopy* **125**, 97–111 (2013).

#### Acknowledgments

**Funding:** X.L. acknowledges the support of Boston University and Boston University Photonics Center. The device fabrication was performed in K. Burch's lab at Boston College. Electrical measurements were conducted at MIT. Y.L. and T.P. acknowledge the partial support by the U.S. Army Research Office through the Institute for Soldier Nanotechnologies, under Cooperative Agreement number W911NF-18-2-0048, AFOSR FATE MURI, grant no. FA9550-15-1-0514, and the STC Center for Integrated Quantum Materials, NSF grant no. DMR 1231319. The TEM imaging was performed at the Center for Nanoscale Systems (CNS), a member of the National Nanotechnology Coordinated Infrastructure Network (NNCI), which is supported by the National Science Foundation under NSF award no. 1541959. CNS is part of Harvard University. **Author contributions:** J.C., T.L., and X.L. conceived and designed the experiments. J.C. and H.G. performed the conversion, optical characterization, and Raman measurements. T.L. performed TEM, STEM, and AFM measurements. T.L. fabricated device. T.L., X.W., and Y.L. conducted electrical measurements supervised by X.L. and T.P. H.W. conducted XPS measurements. J.C., T.L., and X.L. analyzed the data and wrote the manuscript together with input from all authors. **Competing interests:** The authors declare that they have no competing interests. **Data and materials availability:** All data needed to evaluate the conclusions in the paper are present in the paper and/or in the Supplementary Materials. Additional data related to this paper may be requested from the authors.

Submitted 1 May 2019

Accepted 25 October 2019

Published 10 January 2020

10.1126/sciadv.aax8784

**Citation:** J. Cao, T. Li, H. Gao, Y. Lin, X. Wang, H. Wang, T. Palacios, X. Ling, Realization of 2D crystalline metal nitrides via selective atomic substitution. *Sci. Adv.* **6**, eaax8784 (2020).

## Realization of 2D crystalline metal nitrides via selective atomic substitution

Jun Cao, Tianshu Li, Hongze Gao, Yuxuan Lin, Xingzhi Wang, Haozhe Wang, Tomás Palacios and Xi Ling

*Sci Adv* **6** (2), eaax8784.

DOI: 10.1126/sciadv.aax8784

### ARTICLE TOOLS

<http://advances.sciencemag.org/content/6/2/eaax8784>

### SUPPLEMENTARY MATERIALS

<http://advances.sciencemag.org/content/suppl/2020/01/06/6.2.eaax8784.DC1>

### REFERENCES

This article cites 46 articles, 4 of which you can access for free  
<http://advances.sciencemag.org/content/6/2/eaax8784#BIBL>

### PERMISSIONS

<http://www.sciencemag.org/help/reprints-and-permissions>

Use of this article is subject to the [Terms of Service](#)

*Science Advances* (ISSN 2375-2548) is published by the American Association for the Advancement of Science, 1200 New York Avenue NW, Washington, DC 20005. The title *Science Advances* is a registered trademark of AAAS.

Copyright © 2020 The Authors, some rights reserved; exclusive licensee American Association for the Advancement of Science. No claim to original U.S. Government Works. Distributed under a Creative Commons Attribution NonCommercial License 4.0 (CC BY-NC).